Plasmonic Mach–Zehnder Interferometer for Ultrasensitive On-Chip Biosensing

Yongkang Gao,[†] Qiaoqiang Gan,[‡] Zheming Xin,[†] Xuanhong Cheng,[§] and Filbert J. Bartoli[†,*]

[†]Center for Optical Technologies, Electrical and Computer Engineering Department, Lehigh University, Bethlehem, Pennsylvania 18015, United States, [‡]Electrical Engineering Department, University at Buffalo, The State University of New York, Buffalo, New York 14150, United States, and [§]Materials Science and Engineering Department, Bioengineering Program, Lehigh University, Bethlehem, Pennsylvania 18015, United States

ABSTRACT

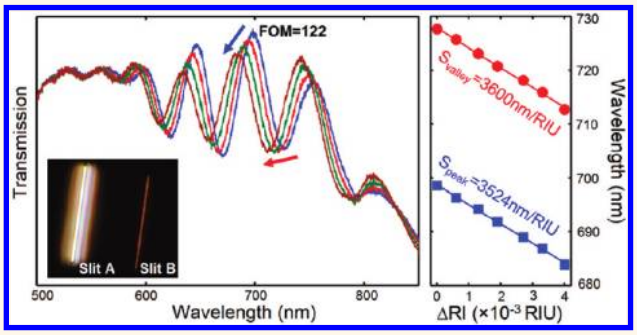

We experimentally demonstrate a plasmonic Mach–Zehnder interferometer (MZI) integrated with a microfluidic chip for ultrasensitive optical biosensing. The MZI is formed by patterning two parallel nanoslits in a thin metal film, and the sensor monitors the phase difference, induced by surface biomolecular adsorptions, between surface plasmon waves propagating on top and bottom surfaces of the metal film. The combination of a nanoplasmonic architecture and sensitive interferometric techniques in this compact sensing platform yields enhanced refractive index sensitivities greater than 3500 nm/RIU and record high sensing figures of merit exceeding 200 in the visible region, greatly surpassing those of previous plasmonic sensors and still hold potential for further improvement through optimization of the device structure. We demonstrate real-time, label-free, quantitative monitoring of streptavidin–biotin specific binding with high signal-to-noise ratio in this simple, ultrasensitive, and miniaturized plasmonic biosensor.

KEYWORDS: biosensing · plasmonics · Mach–Zehnder interferometry · sensitivity · figure of merit

Surface plasmons (SPs) are electromagnetically excited coherent charge oscillations at a metal–dielectric interface.[1] Their optical fields are strongly confined at the metal surface, making them extremely sensitive to changes in the local refractive index, such as those induced by surface biomolecular binding events.[2] This attractive property of SPs is the basis for surface plasmon resonance (SPR) biosensing, which has become the gold standard for high-sensitivity, label-free, real-time monitoring of biomolecular interactions,[3] and has been widely used for biomedical diagnostics, food safety monitoring, and environmental sensing. Most commercial SPR systems employ a prism to couple light into SPs on a flat, continuous metal film in the Kretschmann configuration.[2] While this approach has advantages, the intrinsic size and alignment requirements of prism-based SPR sensors are a significant limitation when compact, low-cost devices are required for high-throughput bioanalytical measurements.[4–7]

Nanoplasmonic sensors, employing nanoparticles or nanostructured metallic films to couple incident light directly into SPs, are an emerging sensing platform that can help overcome the above limitations.[5–8] They permit low-cost, miniaturized, on-chip biosensing in a simple collinear transmission or reflection geometry, raising the potential for high-multiplexing detection without requiring a bulky and complex prism-coupling configuration. Various plasmonic nanostructures have been successfully employed in novel biosensing applications, including catalytic reaction probes,[9] molecular vibrational spectroscopy,[10] enhanced detection of chiral molecules,[11] and live viruses detection.[12] However, the sensitivities and detection limits of nanoplasmonic sensors reported to date are not comparable with commercial prism-based SPR sensors.[5–16] For example, the reported refractive index sensitivities of 300 nm/RIU ($\lambda \sim 800$ nm) for nanoparticles,[13] 560 nm/RIU ($\lambda \sim 900$ nm) for nanoslit arrays,[14] and 313 nm/RIU ($\lambda \sim 700$ nm) for nanohole arrays[15] are 1–2 orders of magnitude lower than those for prism-based SPR systems (13 800 nm/RIU at $\lambda \sim 850$ nm).[16] As a result, increasing the sensitivities of nanoplasmonic biosensors is important for their integration into practical devices and impact on future biosensing markets.

* Address correspondence to fjb205@lehigh.edu.

Received for review September 5, 2011 and accepted November 8, 2011.

Published online November 08, 2011
10.1021/nn2034204

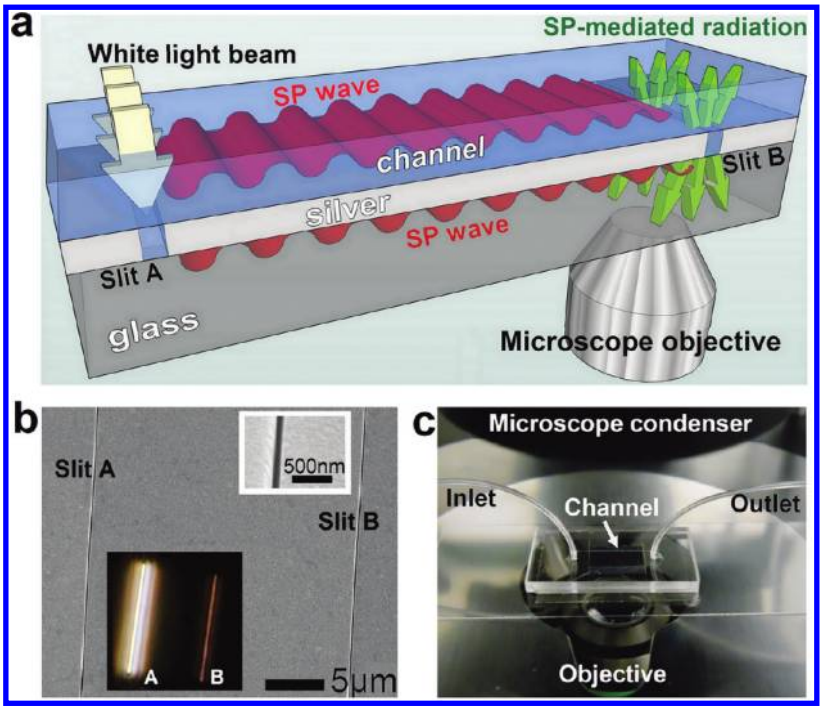

Figure 1. (a) Schematic of the plasmonic MZI. (b) SEM image of a two-nanoslit structure (each slit being 35 μm long and 0.1 μm wide) with a slit separation of 22.7 μm. The top inset shows a detailed SEM image of one nanoslit. The bottom inset shows the transmission image of a two-nanoslit structure with slit A being illuminated. (c) Photograph of the plasmonic MZI integrated with a microfluidic chip.

Optical interferometry is a highly sensitive method for interrogating molecular binding interactions on functional surfaces. It has been applied, for example, to fluorescence interferometry for high-resolution microscopy or nanoscopy,[17,18] as well as label-free sensing based on the Mach–Zehnder interferometer (MZI),[19,20] Young interferometer,[21] dual polarization interferometer,[22] backscattering interferometer,[23] and spectral reflectance interferometer.[24] Surface plasmon interferometry has also been proposed recently[25–28] and suggested as a promising technique for sensitive refractive index sensing.[29,30] In the present work, we demonstrate a compact plasmonic MZI integrated on a microfluidic platform for highly sensitive, label-free, on-chip biosensing. The simple plasmonic MZI architecture, consisting of two parallel nanoslits in a metal film, does not require challenging fabrication methods and is amenable to large-area nanofabrication techniques. Sensing performance of the plasmonic MZI in an aqueous environment was systematically investigated and shows good agreement with theoretical predictions. We experimentally achieved greatly enhanced refractive index sensitivities and record high sensing figures of merit, significantly surpassing that of other non-prism-based plasmonic sensing platforms reported in the visible and near-infrared domain. Theoretical calculations show that further improvement in sensor performance is still possible through rational design and optimization of the device structure. To demonstrate the feasibility of this plasmonic MZI for biosensing, real-time label-free monitoring of protein binding events was successfully performed using simple transmission far-field microscopy. Quantitative information on the effective thickness of the adsorbed protein layer was also extracted from the sensor response based on a simple analytical formalism.

RESULTS AND DISCUSSION

Detection Principle. A schematic illustration of the plasmonic MZI is shown in Figure 1a. The device consists of a 350 nm thick silver film evaporated onto a flat fused silica microscope slide. Focused ion beam milling was used to fabricate a series of double-slit patterns, with slit separation distances of 22.7, 34.2, 45.6, and 57.6 μm. Each slit is 35 μm long and 0.1 μm wide. An SEM image of a slit pair with a slit separation distance of 22.7 μm is shown in Figure 1b, and a photograph of the fabricated plasmonic MZI on a microfludic platform is shown in Figure 1c. Optical measurements were performed using an Olympus IX81 inverted microscope. A white light beam from a 100 W halogen lamp was focused onto the left slit A from the metalized side of the sample (see the lower inset of Figure 1b). Slit A scatters part of the incident radiation into SP modes in both sensing and reference arms, located at the top metal surface and buried bottom metal/substrate interface, respectively (see Figure 1a). The SP waves launched in these two arms propagate toward the right slit B, where they interfere with each other and modulate the far-field scattering.

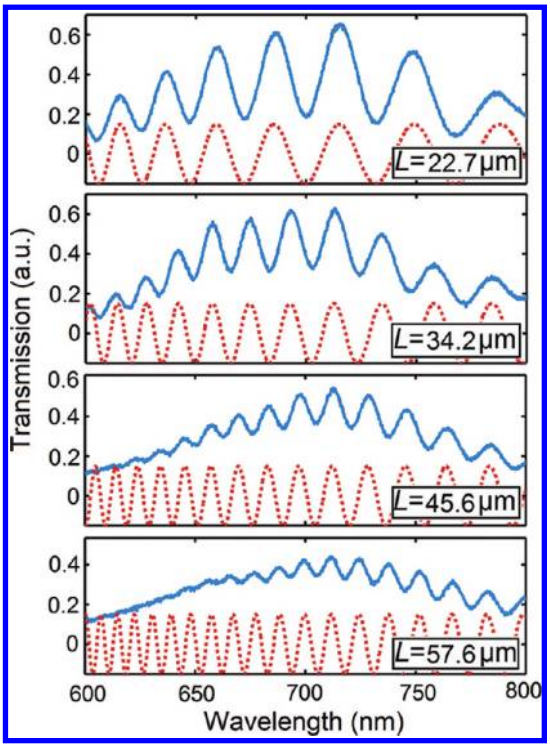

Figure 2. Experimental SP-mediated interference patterns for two-nanoslit structures in an air environment with slit separation distances, *L*, of 22.7, 34.2, 45.6, and 57.6 μm (from top to bottom). The top spectra (solid curves) are experimental spectra, and the lower dotted curves are theoretical predictions. No smoothing algorithm was applied to the experimental spectra.

The SP-mediated radiation from slit B was collected in transmission mode by an X40 microscope objective to measure the spectral interference patterns. For a specific wavelength, the intensity of the far-field transmission depends on the phase difference between the two SP waves at the top sensing surface and bottom reference surface, which is modulated when biomolecules are adsorbed on the sensing metal surface. For broad-band illumination, a spectral shift of the interference pattern would be observed. Note that the sensing and reference arms of this plasmonic MZI are vertically aligned and separated by a 350 nm thick thin silver film, enabling a compact footprint and dense array packing. The silver film also serves as a protection layer for the buried reference arm, eliminating the need for additional cladding layer deposition and etching procedures as required for planar waveguide MZI.[19] The simplicity, compactness, and ease-of-fabrication of this plasmonic sensing platform make it attractive for integration into practical, cost-effective sensing devices with potential high-multiplexing capability.

The solid curves in Figure 2 show the experimental spectra for a series of plasmonic MZIs in an air environment, with different slit separation distances *L*. The experiment was configured in a way that only SP-mediated far-field scattering contributes to the resulting spectral oscillations (see Methods). Obvious interference patterns are observed as a function of wavelength under TM polarized illumination (with the electric field perpendicular to the long axis of the slit). For samples with larger *L*, the amplitudes of the interference oscillations are smaller, indicating increased SP propagation loss at the metal surfaces. The decreased visibility of the interference is related to the increasing intensity imbalance between the signals in two arms, as SPs experience greater propagation loss at the silver/glass interface. In this work, we focus on the spectral positions of the interference peaks and valleys and their usefulness for biosensing. To better interpret the measurements, theoretical interference patterns were calculated using the equation

$$I \propto \cos\left[\frac{2\pi L}{\lambda}(n_{sp1}(\lambda) - n_{sp2}(\lambda)) + \varphi_0\right] \quad (1)$$

Here $n_{spi}(\lambda) = \mathrm{Re}(((\varepsilon_m(\lambda)n_i^2)/(\varepsilon_m(\lambda)+n_i^2))^{1/2})$ is the effective refractive index of SP at the metal/dielectric interface, ε_m is the metal permittivity, n_i is the refractive index of the dielectric, and the subscript $i = 1, 2$ denotes the upper dielectric and lower glass substrate, respectively. φ_0 is an additional constant phase shift.[27] Using $n_1 = 1.00$ for air, the calculated interference patterns show a higher oscillation frequency than the experimental data, consistent with the results reported previously in refs 25, 26, and 28. This discrepancy is attributed to formation of a contamination layer of Ag_2S (or a mixture of Ag_2O/AgO) on top of the silver surface.[25,28] Here we assume a contamination film thickness of 4 nm (consistent with exposure in air for several weeks)[31] and a film refractive index of 2.8,[32,33] which yields an effective refractive index of the top dielectric $n_1 = 1.03$. One can see from Figure 2 that the resulting calculated oscillation frequencies and spectral positions of the peaks and valleys (dotted curves) agree very well with the measured data for plasmonic MZIs with four different *L*.

Sensitivity Calibration. The spectral interrogation sensitivity of the plasmonic MZI can be derived from eq 1 by setting the term $[n_{sp1}(\lambda) - n_{sp2}(\lambda)]/\lambda$ to be constant, yielding

$$S = \left|\frac{\Delta\lambda}{\Delta n}\right| \approx \lambda\left(\frac{n_{sp1}(\lambda)}{n_1}\right)^3 \Big/ \left[\Delta n_{sp21}(\lambda) - \lambda\frac{d\Delta n_{sp21}}{d\lambda}\right] \quad (2)$$

where $\Delta n_{sp21}(\lambda) = n_{sp2}(\lambda) - n_{sp1}(\lambda)$. The bulk refractive index sensitivity, *S*, depends directly on the operational wavelength, the dielectric properties of the metal, and the refractive indices of the dielectrics at the upper and lower interfaces. For a liquid environment ($n_1 = 1.330$, $n_2 = 1.516$), this equation predicts *S* is greater than 3000 nm/RIU in the visible region. This sensitivity level is significantly higher than those of previously reported nanoplasmonic sensors.[5−8] To confirm this theoretical prediction experimentally, a

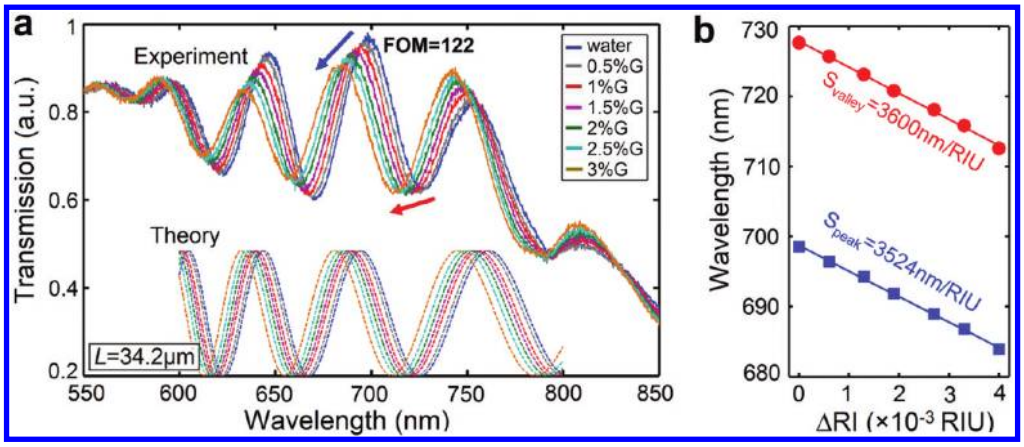

Figure 3. (a) Measured spectra (top curves) and calculated interference patterns (bottom dotted curves) of plasmonic MZI with L = 34.2 μm for water and glycerol−water solutions with six different glycerol volume concentrations (from 0.5 to 3%). The directions of the top and bottom arrows indicate the blue shifts of the peak and the valley. No smoothing algorithm was applied. (b) Spectral positions of the interference peak (squares) and valley (dots) *versus* refractive index of the solutions. The solid lines are linear fits to the data.

double-slit structure with L = 34.2 μm was fabricated and integrated with a PDMS microfluidic channel (see Figure 1c). Glycerol−water solutions of varying glycerol concentration were injected to tune the refractive indices of the liquid. As shown in Figure 3a, the interference pattern blue shifts as the liquid refractive index increases, in good agreement with the theoretical predictions (lower dotted curves). The peak and valley positions of the interference patterns around 700 and 730 nm (indicated by the top and bottom arrows, respectively) were measured as a function of the liquid refractive index and are plotted in Figure 3b. One can see that the positions of the peaks and the valleys vary approximately linearly with the refractive index of the liquid. The sensitivities are estimated to be 3524 nm/RIU (peak) and 3600 nm/RIU (valley) from the linear fits to the experimental data, in agreement with the theoretical predictions obtained using eq 2 (3448 and 3545 nm/RIU at 700 and 730 nm, respectively). These measured refractive index sensitivities are 1 order of magnitude larger than those reported previously for nanoplasmonic sensors based on nanoparticles,[5−8] metamaterials,[34] and extraordinary optical transmission (EOT) through nanoaperture arrays[14,15] in this visible spectral region. In addition, the unique plasmonic interferometry scheme allows broad-band coupling of light into SPs for biosensing. The availability of multiple interference maxima and minima enables this plasmonic MZI sensor to operate at different wavelengths where the SP penetration depth into the liquid environment may vary, permitting the detection of species with different size or/and absorption properties in a single device. With SP fields extending different distances into the liquid, surface and solution refractive index changes may also be distinguished in a single measurement and at a single sensing spot, well-suited for applications in which solution index and compositions are poorly known. The shift of multiple peaks and valleys potentially provides sensor performance superior to that of common single peak monitoring since the sensor response may be integrated over the entire spectrum.[35] This multispectral analysis method is under investigation for the plasmonic MZI and will be reported elsewhere.

The Figure of Merit of Plasmonic MZIs. Equation 2 predicts that the sensor sensitivity can be increased further if n_{sp1} and n_{sp2} are closer in value. This can be realized by matching the refractive indices of the substrate and the top dielectric material. By setting the substrate refractive index n_2 = 1.38 (*e.g.*, using magnesium fluoride as the substrate), a sensitivity of more than 10 000 nm/RIU is potentially achievable at a wavelength of 700 nm in a water environment (n_1 = 1.33). This would greatly surpass the performance of previous nanoplasmonic sensors and compare favorably with prism-based SPR sensors. However, it should be noted that when the two terms are closer in value the oscillation period of the interference pattern also increases, as described by the following expression:

$$P \approx \lambda^2/L\left[\Delta n_{sp21}(\lambda) - \lambda\frac{d\Delta n_{sp21}}{d\lambda}\right] \qquad (3)$$

When $n_{sp1} \approx n_{sp2}$, broadening in the interference pattern makes it difficult to resolve very small wavelength shifts of the peak or valley. To evaluate the performance of plasmonic sensors more precisely, researchers introduced the figure of merit FOM = $(\Delta\lambda/\Delta n)/\delta\lambda$ that simultaneously considers the refractive index sensitivity and the sharpness of the SP resonance.[13,36] Here $\Delta\lambda/\Delta n$ is the refractive index sensitivity and $\delta\lambda$ is the full width at half-maximum (fwhm) of the sensing peak. The FOM of our plasmonic MZI (for L = 34.2 μm) is found experimentally to be 122 (3524 nm/RIU/29 nm) for the interference peak (indicated by the top arrow in Figure 3a). This FOM value is among the highest reported for plasmonic

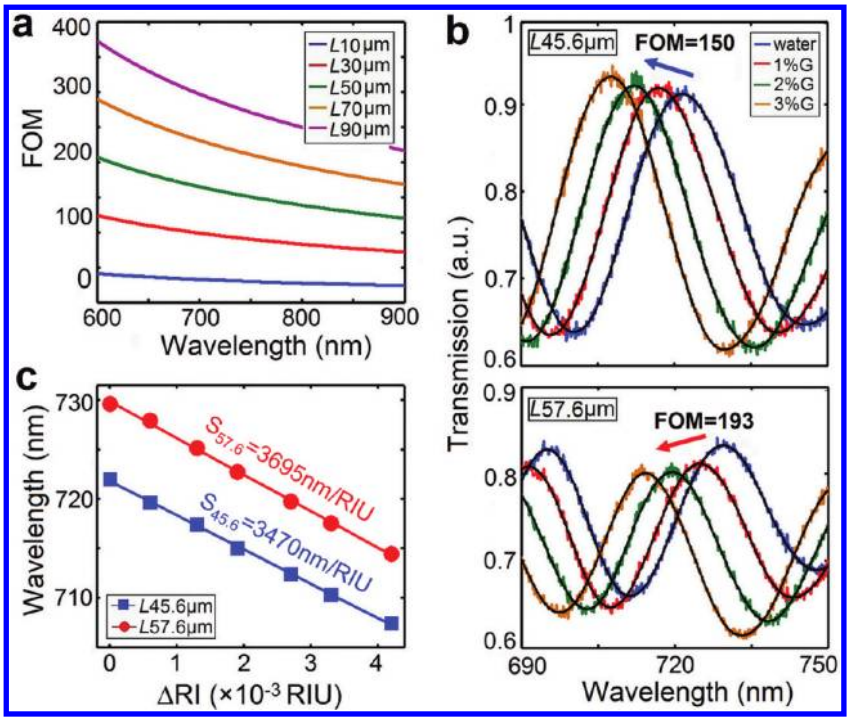

Figure 4. (a) Calculated FOM of the plasmonic MZI as a function of wavelength for values of *L* ranging from 10 to 90 μm. (b) Measured spectra for glycerol–water solutions with varying glycerol volume concentrations. For clarity, only the spectra of water and 1, 2, and 3% glycerol–water solutions were shown. The black curves imposed on the experimental spectra are guides to the eye, obtained using a fast Fourier transform technique to filter out the high-frequency noise of the raw data. Results are shown for *L* = 45.6 and 57.6 μm. (c) Spectral positions of the interference peak *versus* refractive index of the solution. Sensitivities are obtained using a linear fit to the experimental data.

sensors in the visible region.[37] Moreover, the FOM for this plasmonic MZI can be increased further by properly choosing the operational wavelength and slit separation distance *L*. By letting the interference fringe width $\delta\lambda$ be equal to half of the oscillation period *P*, one can easily derive the FOM of plasmonic MZIs from eqs 2 and 3

$$\mathrm{FOM} = \frac{S}{\delta\lambda} = \frac{2S}{P} \approx \frac{2L}{\lambda}\left(\frac{n_{sp1}(\lambda)}{n_1}\right)^3 \qquad (4)$$

Using eq 4, one can estimate the sensor FOM for our plasmonic MZI at *L* = 34.2 μm to be 113, which is in reasonable agreement with the experimentally derived value. Figure 4a shows the calculated FOM as a function of wavelength for different *L*. The results suggest that the value of FOM would increase further for shorter λ or larger *L*.

To demonstrate this theoretical prediction, plasmonic MZIs with *L* = 45.6 and 57.6 μm were fabricated and integrated with microfluidic channels. As shown in Figure 4b, the line width of the interference peak decreases with increasing *L* for the plasmonic MZI in a water environment, consistent with predictions based on eq 3. Liquids with varying refractive index were then injected into the channel, and the peak positions were extracted and plotted in Figure 4c as a function of the liquid refractive index. For plasmonic MZIs with *L* = 45.6 and 57.6 μm, the measured refractive index sensitivities are 3470 and 3695 nm/RIU, respectively, and the resulting FOMs are 150 and 193, respectively, all in good agreement with the theoretical calculations (see Table 1). The achieved FOMs of 193 exceeds all reported FOMs of previous non-prism-based plasmonic sensors in the visible region: the FOM is 23 for sensors based on EOT in nanohole arrays,[15] 14.5 for silver nanowell array based sensors,[38] typically <10 for localized SPR sensors based on nanoparticles,[5–8] 3.8 for metamaterial-based sensor,[34] and 162 for high optical quality nanohole array sensors using subradiant dark modes.[37] Our experimental FOM also surpasses the theoretically estimated FOM value of ≈108

TABLE 1. Experimental and Calculated Sensor Sensitivities, Peak Line Widths, and FOMs for Plasmonic MZIs with Different *L* (Numbers in Italics Are the Theoretically Calculated Values)

L (μm)	peak λ (nm)	sensitivity (nm/RIU)	line width (nm)	FOM
34.2	698	3524	29.0	122
		3442	*30.4*	*113*
45.6	722	3470	23.1	150
		3520	*24.4*	*144*
57.6	730	3695	19.1	193
		3545	*19.7*	*180*
69.0	734	3688	16.5	224
		3558	*16.7*	*213*

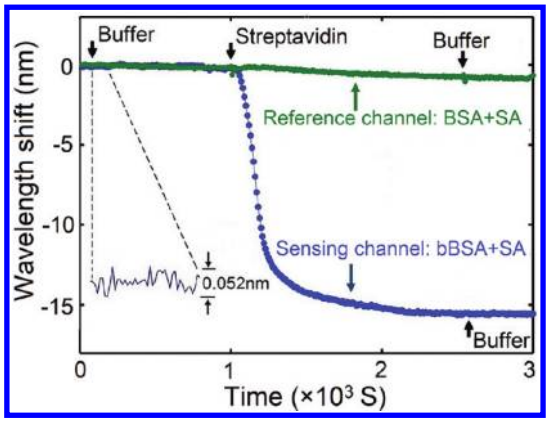

Figure 5. Real-time sensor response upon the adsorption of molecules for biotin-SA sensing experiment (sensing channel) and BSA-SA experiment (reference channel). The inset shows the peak wavelength fluctuations in biotin-SA sensing experiment, which correspond to an inherent noise level of 0.052 nm of the sensing system.

for prism-based SPR sensors.[37,39] While further FOM improvements are still possible for plasmonic MZIs with larger L (for example, a FOM of 224 has also been achieved as shown in Figure S1 in the Supporting Information), the higher propagation loss of SPs results in a decreased spectral modulation depth and lower signal-to-noise ratio, limiting the further enhancement of the overall sensor performance for practical applications. This limitation could potentially be alleviated through several methods. First, the use of ultrasmooth metal films reported recently could decrease the scattering loss of propagating SPs and enhance the sensor signal-to-noise ratio.[40−42] Second, slit dimensions can be optimized[28] to enhance the coupling from light to SPs at the nanoslit. Further optimization of the plasmonic MZI performance is still under investigation. With demonstrated enhanced sensor performance and the potential for further improvements, this simple plasmonic MZI platform is promising for practical ultrasensitive integrated biosensing systems.

Biosensing Experiments. To examine the feasibility of this plasmonic MZI platform for real-time label-free biosensing, we employ the streptavidin−biotin affinity binding model. Measurements were performed using the same plasmonic MZI (L = 34.2 μm) discussed above in the bulk sensitivity calibration experiments. The sensor surface was first functionalized with a monolayer of biotinylated bovine serum albumin (bBSA). HEPES buffer was then injected into the channel at a flow rate of 20 μL/min and run for 20 min to define the baseline of the experiment. We then focused on the interference peak around 690 nm (data not shown here) and recorded its spectral position in real-time using a Lorentzian peak fitting method. As shown by the lower data points in Figure 5, the injection of a 300 nM (16 μg/mL) streptavidin (SA) solution generated a large peak shift of 15.7 nm. A subsequent buffer rinsing had little effect on the peak wavelength. To rule out nonspecific binding of the analyte, a control experiment was also performed, in which a 300 nM SA solution was injected into a reference channel, whose sensor surface was covered by a monolayer of BSA without biotin conjugation. This was followed by a buffer rinse. A very small blue shift of the peak (0.7 nm) is observed (see the upper data points in Figure 5), possibly due to nonspecific binding events. The net peak shift of 15 nm is therefore associated with the specific binding of biotin and SA. This value is considerably larger than previously reported results (*e.g.*, 3.8 nm for 370 nM SA in gold nanodot arrays,[43] 6 nm for 370 nM SA in nanoparticle arrays,[44] 3.5−4 nm for 5 μM SA in gold nanohole arrays,[45] and 2−4 nm for 2 μM SA in a single gold nanoparticle platform).[46]

Next, we quantitatively extract the effective protein layer thickness d_e for streptavidin from the peak wavelength shift $\Delta\lambda$ using the simple expression[47]

$$\Delta\lambda = S(n_l - n_b)(1 - e^{-2d_e/l_d}) \quad (5)$$

where S is the bulk sensitivity determined from the calibration experiment (S = 3524 nm/RIU), and n_l and n_b are the refractive indices of the adsorbed protein layer and buffer solution, respectively; l_d is the decay length of SPs into the solution, which is calculated to be 310 nm at 690 nm. If one assumes the effective refractive index of protein is n = 1.5, the wavelength shift of 15 nm upon adsorption of SA protein layer corresponds to a calculated effective thickness of 3.9 nm for the SA layer, which agrees with the literature values for a SA monolayer.[35,48]

The fluctuations in the sensor response determine the noise level of our biosensor system. As shown in the lower inset of Figure 5, an inherent noise of 0.052 nm was obtained, which represents twice the standard deviation (2σ) of the monitored peak wavelength. This system noise corresponds to a sensor detection limit of 1.5×10^{-5} RIU [0.052 nm/(3524 nm/RIU)] and a high signal-to-noise ratio of 288 for monolayer SA binding. It is worth mentioning that no temperature control was employed in these experiments. Temperature fluctuations of around 0.1 K in water would be expected to cause a refractive index change of $\sim 1 \times 10^{-5}$ RIU.[49] Further improvement in sensor detection limit and signal-to-noise ratio would be expected by optimizing the device structure, developing advanced data analysis methods, and using temperature control and lower-noise light source and detection systems.

CONCLUSIONS

In conclusion, we experimentally demonstrate a plasmonic MZI for miniaturized and ultrasensitive optical biosensing. The combination of sensitive interferometric techniques with nanoplasmonic architectures yields greatly enhanced sensitivities and record high figures of merit in a simple and compact sensor

platform. The feasibility of this plasmonic interferometer for real-time, label-free, quantitative biosensing was also demonstrated by monitoring of protein binding events using simple transmission spectroscopy, significantly decreasing the sensing system complexity compared to conventional SPR measurements. The demonstrated enhanced sensor performance makes this miniaturized device promising for practical integrated biosensing platforms and subwavelength optics on-a-chip.

METHODS

Fabrication of Plasmonic MZI. Silver films of 350 nm thickness were deposited by e-beam evaporation (Indel system) onto flat fused silica microscope slides (Fisherbrand). Prior to the evaporation, the glass slides were cleaned thoroughly with acetone in an ultrasonic cleaner for 20 min, followed by extensive DI water rinsing. Focused ion beam (FEI Dual-Beam system 235) milling (30 kV, 30pA) was used to fabricate the double-slit plasmonic MZI structures.

Optical Measurements. A 100 W halogen lamp was used to illuminate the double-slit patterns through the microscope condenser of an Olympus IX81 inverted microscope. The condenser centering screws were tuned to move the image of the field diaphragm off the center of the viewing area, illuminating only the left slit A (with the right slit B located at the center of the viewing area). The transmitted light emanating from the slits was collected by a X40 microscope objective (NA = 0.6) and passed through an iris diaphragm that ensures only the SP-mediated radiation from slit B in the center was transmitted. This signal was coupled into a multimode fiber bundle interfaced to a fiber-based compact spectrometer (Ocean Optics USB 4000). When slit A is illuminated and scattered light collected from slit B, the SP-mediated far-field scattering is directly observed. However, the measured data also contain a weak radiation leakage emanating directly from two open slits. Consequently, we designed another control experiment to remove the light leakage and to emphasize the SP contribution. A CCD camera (Cooke sensicam qe) was employed to record the positions of the double slits. Under identical experimental conditions, a reference single slit was moved to the recorded positions of the left and then the right slit of the interferometer. The collected transmission spectra were then both subtracted from the experimental raw data to yield the SP-mediated far-field scattering spectra shown in Figure 2. Each spectrum shown in this work represents an average of 100 acquisitions with an integration time of 100 ms for each acquisition.

Theoretical Calculations. Equation 1 was used to plot the theoretical interference patterns shown in Figures 2 and 3, using values for the permittivity of silver obtained from ref 50. Silver is known to corrode in air due to its reaction with oxygen and sulfur. Here we assume a contamination layer thickness of 4 nm with a refractive index of 2.8. This corresponds to an effective refractive index for the upper dielectric material of $n_{eff} = n_1 =$ 1.03 in air and 1.37 in water. This assumption provides a good agreement between experimental data and theoretical predictions for plasmonic MZI in both air and aqueous environments; $n_{eff} = n_1 = 1.37$ was also used with eq 2, 3, and 4 to calculate the sensitivity, line width, and the FOM of the plasmonic MZI, all in good agreement with the experimental results. The additional phase shift in eq 1 can be written as $\varphi_0 = \varphi_1 - \varphi_2$, where φ_1 and φ_2 are the phase shifts associated with the scattering and transmission of the two SP waves at the slits. The values of φ_0 used in calculations were obtained by fitting the experimental spectra using eq 1. The values of φ_0 used are 0.78π, 0.64π, 0.25π, and 0.80π (for $L = 22.7$, 34.2, 45.6, and 57.6 μm, respectively) in air environment (Figure 2) and 0.96π for $L = 34.2$ μm in water (Figure 3). Note that the key focus in the comparison between experimental and theoretical results in this work is the spectral positions of the peaks and valleys and their spectral shifts upon changes in n_1 since this plasmonic sensing scheme is based on spectral interrogation. It is difficult to predict the amplitudes of the interference patterns accurately, which requires detailed information about the SP propagation loss and coupling efficiencies between SPs and free space light. This near-field information is difficult to determine from the experiments performed in this work.

Fabrication of PDMS Microfluidic Channels. Microfluidic channels were fabricated by conventional soft lithography. A SU-8 (SU8–50, Microchem) master mold of the channel (50 μm deep and 4 mm wide) was patterned on a 3 in. wafer by photolithography. A 10:1 ratio of PDMS (Sylgard 184, Dow corning) and curing agent was used to cast the mold, which was then baked at 70 °C for 3 h. The PDMS channel was cut and peeled from the master, and inlet and outlet holes were punched for tubing. The surfaces of the microfluidic channel and the nanopatterned sample were then activated by oxygen plasma treatment (PX-250, March Instruments) and bonded to each other.

Bulk Sensitivity Calibration and Biosensing Experiments. To calibrate the sensitivity of plasmonic MZI, glycerol–water solutions were prepared with glycerol volume concentrations varying from 0.5 to 3%. An ellipsometer (J.A. Woollam, V-VASE) was used to measure their refractive indices, which range from $n = 1.3302$ to $n = 1.3344$. A 10 mM HEPES buffer (Sigma-Aldrich) was prepared and adjusted to pH 7.4. Solutions were injected into the microfluidic channel using a syringe pump (Harvard Apparatus) at a flow rate of 20 μL/min. For biotin-SA sensing experiments, 500 μg/mL biotinylated BSA (Thermal Scientific) was first injected and run for 20 min to functionalize the sensor surface with a monolayer of bBSA. In the control experiment, 500 μg/mL BSA (Thermal Scientific) was injected into the reference channel and run for 20 min to form a BSA monolayer. Streptavidin (Piece, USA) was prepared at a concentration of 300 nM (16 μg/mL) and run for 27 min in both sensing and control experiments. Interference patterns were continuously recorded with a temporal resolution of 10 s as solutions were flowed over the sensor surface.

Acknowledgment. This work was supported by the National Science Foundation grant (CBET-1014957). Q.G. acknowledges financial support from National Science Foundation grant (ECCS-1128086). We thank Shu-Han Wu and Krissada Surawathanawises for their help in sample processing, and Yunseong Jeon and Sabrina Jedlicka for their helpful discussions.

Supporting Information Available: Further optimization of the plasmonic MZI sensor performance. This material is available free of charge *via* the Internet at http://pubs.acs.org.

REFERENCES AND NOTES

1. Ritchie, R. H. Plasma Losses by Fast Electrons in Thin Films. *Phys. Rev.* **1957**, *106*, 874–881.
2. Maier, S. A. In *Plasmonics: Fundamentals and Applications*; Springer: New York, 2007.
3. Homola, J. Surface Plasmon Resonance Sensors for Detection of Chemical and Biological Species. *Chem. Rev.* **2008**, *108*, 462–493.
4. Yan, R.; Mestas, S. P.; Yuan, G.; Safaisini, R.; Dandy, D. S.; Lear, K. L. Label-Free Silicon Photonic Biosensor System with Integrated Detector Array. *Lab Chip* **2009**, *9*, 2163–2168.
5. Anker, J. N.; Hall, W. P.; Lyandres, O.; Shan, N. C.; Zhao, J.; Van Duyne, R. P. Biosensing with Plasmonic Nanosensors. *Nat. Mater.* **2008**, *7*, 442–453.
6. Stewart, M. E.; Anderton, C. R.; Thompson, L. B.; Maria, J.; Gray, S. K.; Rogers, J. A.; Nuzzo, R. G. Nanostructured Plasmonic Sensors. *Chem. Rev.* **2008**, *108*, 494–521.

7. Lal, S.; Link, S.; Halas, N. J. Nano-Optics from Sensing to Waveguiding. *Nat. Photonics* **2007**, *1*, 641–648.
8. Mayer, K. M.; Hafner, J. H. Localized Surface Plasmon Resonance Sensors. *Chem. Rev.* **2011**, *111*, 3828–3857.
9. Larsson, E. M.; Langhammer, C.; Zoric, I.; Kasemo, B. Nanoplasmonic Probes of Catalytic Reactions. *Science* **2009**, *326*, 1091–1094.
10. Adato, R.; Yanik, A. A.; Amsden, J. J.; Kaplan, D. L.; Omenetto, F. G.; Hong, M. K.; Erramilli, S.; Altug, H. Ultra-sensitive Vibrational Spectroscopy of Protein Monolayers with Plasmonic Nanoantenna Arrays. *Proc. Natl. Acad. Sci. U.S.A.* **2009**, *106*, 19227–19232.
11. Hendry, E.; Carpy, T.; Johnston, J.; Popland, M.; Mikhaylovskiy, R. V.; Lapthorn, A. J.; Kelly, S. M.; Barron, L. D.; Gadegaard, N.; Kadodwala, M. Ultrasensitive Detection and Characterization of Biomolecules using Superchiral Fields. *Nat. Nanotechnol.* **2010**, *5*, 783–787.
12. Yanik, A. A.; Huang, M.; Kamohara, O.; Artar, A.; Geisbert, T. W.; Connor, J. H.; Altug, H. An Optofluidic Nanoplasmonic Biosensor for Direct Detection of Live Viruses from Biological Media. *Nano Lett.* **2010**, *10*, 4962–4969.
13. Otte, A. M.; Sepulveda, B.; Ni, W.; Juste, J. P.; Liz-Marzan, L. M.; Lechuga, L. M. Identification of the Optimal Spectral Region for Plasmonic and Nanoplasmonic Sensing. *ACS Nano* **2010**, *4*, 349–357.
14. Lee, M. H.; Gao, H.; Odom, T. W. Refractive Index Sensing Using Quasi One-Dimensional Nanoslit Arrays. *Nano Lett.* **2009**, *9*, 2584–2588.
15. Henzie, J.; Lee, M. H.; Odom, T. W. Multiscale Patterning of Plasmonic Metamaterials. *Nat. Nanotechnol.* **2007**, *2*, 549–554.
16. Homola, J.; Yee, S. S.; Gauglitz, G. Surface Plasmon Resonance Sensors: Review. *Sens. Actuators, B* **1999**, *54*, 3–15.
17. Moiseev, L.; Unlü, M. S.; Swan, A. K.; Goldberg, B. B.; Cantor, C. R. DNA Conformation on Surfaces Measured by Fluorescence Self-Interference. *Proc. Natl. Acad. Sci. U.S.A.* **2006**, *103*, 2623–2628.
18. Bilenca, A.; Cao, J.; Colice, M.; Ozcan, A.; Bouma, B.; Raftery, L.; Tearney, G. Fluorescence Interferometry: Principles and Applications in Biology. *Ann. N.Y. Acad. Sci.* **2008**, *1130*, 68–77.
19. Prieto, F.; Sepulveda, B.; Calle, A.; Llobera, A.; Dominguez, C.; Abad, A.; Montoya, A.; Lechuga, L. M. An Integrated Optical Interferometric Nanodevice Based on Silicon Technology for Biosensor Applications. *Nanotechnology* **2003**, *14*, 907–912.
20. Lapsley, M. I.; Chiang, I.-K.; Zheng, Y.; Ding, X.; Mao, X.; Huang, T. J. A Single-Layer, Planar, Optofluidic Mach-Zehnder Interferometer for Label-Free Detection. *Lab Chip* **2011**, *11*, 1795–1800.
21. Ymeti, A.; Kanger, J. S.; Greve, J.; Lambeck, P. V.; Wijn, R.; Heideman, R. G. Realization of a Multichannel Integrated Young Interferometer Chemical Sensor. *Appl. Opt.* **2003**, *42*, 5649–5660.
22. Swann, M. J.; Peel, L. L.; Carrington, S.; Freeman, N. J. Dual-Polarization Interferometry: An Analytical Technique To Measure Changes in Real Time, To Determine the Stoichiometry of Binding Events, and To Differentiate between Specific and Nonspecific Interactions. *Anal. Biochem.* **2004**, *329*, 190–198.
23. Bornhop, D. J.; Latham, J. C.; Kussrow, A.; Markov, D. A.; Jones, R. D.; Sørensen, H. S. Free-Solution, Label-Free Molecular Interactions Studied by Back-Scattering Interferometry. *Science* **2007**, *317*, 1732–1736.
24. Ozkumur, E.; Needham, J. W.; Bergstein, D. A.; Gonzalez, R.; Cabodi, M.; Gershoni, J. M.; Goldberg, B. B.; Unlü, M. S. Label-Free and Dynamic Detection of Biomolecular Interactions for High-Throughput Microarray Applications. *Proc. Natl. Acad. Sci. U.S.A.* **2008**, *105*, 7988–7992.
25. Lalanne, P; Hugonin, J. P. Interaction between Optical Nano-Objects at Metallo-Dielectric Interfaces. *Nat. Phys.* **2006**, *2*, 551–556.
26. Gay, G.; Alloschery, O.; Viaris De Lesegno, B.; Dwyer, C. O'.; Weiner, J.; Lezec, H. J. The Optical Response of Nanostructured Surfaces and the Composite Diffracted Evanescent Wave Model. *Nat. Phys.* **2006**, *2*, 262–267.
27. Schouten, H. F.; Kuzmin, N.; Dubois, G.; Visser, T. D.; Gbur, G.; Alkemade, P. F. A.; Blok, H.; Hooft, G. W.'t; Lenstra, D.; Eliel, E. R. Plasmon-Assisted Two-Slit Transmission: Young's Experiment Revisited. *Phys. Rev. Lett.* **2005**, *94*, 053901-4.
28. Gan, Q.; Gao, Y.; Wang, Q.; Zhu, L.; Bartoli, F. J. Surface Plasmon Waves Generated by Nanogrooves through Spectral Interference. *Phys. Rev. B* **2010**, *81*, 085443-5.
29. Gan, Q.; Gao, Y.; Bartoli, F. J. Vertical Plasmonic Mach–Zehnder Interferometer for Sensitive Optical Sensing. *Opt. Express* **2009**, *17*, 20747–20755.
30. Wu, X.; Zhang, J.; Chen, J.; Zhao, C.; Gong, Q. Refractive Index Sensor Based on Surface-Plasmon Interference. *Opt. Lett.* **2009**, *34*, 392–394.
31. Bennett, H. E.; Peck, R. L.; Burge, D. K.; Bennett., J. M. Formation and Growth of Tarnish on Evaporated Silver Films. *J. Appl. Phys.* **1969**, *40*, 3351–3360.
32. Bennett, J. M.; Stanford, J. L.; Ashley, E. J. Optical Constants of Silver Sulfide Tarnish Films. *J. Opt. Soc. Am.* **1970**, *60*, 224–231.
33. Tominaga, J. The Application of Silver Oxide Thin Films to Plasmon Photonic Devices. *J. Phys.: Condens. Matter* **2003**, *15*, R1101–R1122.
34. Liu, N.; Weiss, T.; Mesch, M.; Langguth, L.; Eigenthaler, U.; Hirscher, M.; Sonnichsen, C.; Giessen, H. Planar Metamaterial Analogue of Electromagnetically Induced Transparency for Plasmonic Sensing. *Nano Lett.* **2010**, *10*, 1103–1107.
35. Stewart, M. E.; Mack, N. H.; Malyarchuk, V.; Soares, J. A. N. T.; Lee, T. W.; Gray, S. K.; Nuzzo, R. G.; Rogers, J. A. Quantitative Multispectral Biosensing and 1D Imaging Using Quasi-3D Plasmonic Crystals. *Proc. Natl. Acad. Sci. U.S.A.* **2006**, *103*, 17143–17148.
36. Sherry, L. J.; Chang, S. H.; Schatz, G. C.; Van Duyne, R. P.; Wiley, B. J.; Xia, Y. Localized Surface Plasmon Resonance Spectroscopy of Single Silver Nanocubes. *Nano Lett.* **2005**, *5*, 2034–2038.
37. Yanik, A. A.; Cetin, A. E.; Huang, M.; Artar, A.; Hossein Mousavi, S.; Khanikaev, A.; Connor, J. H.; Shvets, G.; Altug, H. Seeing Protein Monolayers with Naked Eye through Plasmonic Fano Resonances. *Proc. Natl. Acad. Sci. U.S.A.* **2011**, *108*, 11784–11789.
38. Hicks, E. M.; Zhang, X.; Zou, S.; Lyandres, O.; Spears, K. G.; Schatz, G. C.; Van Duyne, R. P. Plasmonic Properties of Film over Nanowell Surfaces Fabricated by Nanosphere Lithography. *J. Phys. Chem. B* **2005**, *109*, 22351–22358.
39. Tetz, K. A.; Pang, L; Fainman, Y. High-Resolution Surface Plasmon Resonance Sensor based on Linewidth-Optimized Nanohole Array Transmittance. *Opt. Lett.* **2006**, *31*, 1528–1530.
40. Nagpal, P.; Lindquist, N. C.; Oh, S.; Norris, D. J. Ultrasmooth Patterned Metals for Plasmonics and Metamaterials. *Science* **2009**, *325*, 594–597.
41. Zhu, X.; Zhang, Y.; Zhang, J.; Xu, J.; Ma, Y.; Li, Z.; Yu, D. Ultrafine and Smooth Full Metal Nanostructures for Plasmonics. *Adv. Mater.* **2010**, *22*, 4345–4349.
42. Im, H.; Lee, S. H.; Wittenberg, N. J.; Johnson, T. W.; Lindquist, N. C.; Prashant, N.; Norris, D. J.; Oh, S.-H. Template-Stripped Smooth Ag Nanohole Arrays with Silica Shells for Surface Plasmon Resonance Biosensing. *ACS Nano* **2011**, *5*, 6244–6253.
43. Vazquez-Mena, O.; Sannomiya, T.; Villanueva, L. G.; Voros, J.; Brugger, J. Metallic Nanodot Arrays by Stencil Lithography for Plasmonic Biosensing Applications. *ACS Nano* **2011**, *5*, 844–853.
44. Sannomiya, T; Sahoo, P. K.; Solak, D. I.; Hafner, H. H.; Grieshaber, C.; Voros, D. Biosensing by Densely Packed and Optically Coupled Plasmonic Particle Arrays. *Small* **2009**, *5*, 1889–1896.
45. Leebeeck, A. D.; Swaroop Kumar, L. K.; Lange, V. D.; Sinton, D.; Gordon, R.; Brolo, A. G. On-Chip Surface-Based Detection with Nanohole Arrays. *Anal. Chem.* **2007**, *79*, 4094–4100.
46. Raschke, G.; Kowarik, S.; Franzl, T.; Sönnichsen, C.; Klar, T. A.; Feldmann, J.; Nichtl, A.; Kurizinger, K. Biomolecular

Recognition Based on Single Gold Nanoparticle Light Scattering. *Nano Lett.* **2003**, *3*, 935–938.
47. Jung, L. S.; Campbell, C. T.; Chinowsky, T. M.; Mar, M. N.; Yee, S. S. Quantitative Interpretation of the Response of Surface Plasmon Resonance Sensors to Adsorbed Films. *Langmuir* **1998**, *14*, 5636–5648.
48. Haussling, L.; Ringsdorf, H.; Schmitt, F. J.; Knoll, W. Biotin-Functionalized Self-Assembled Monolayers on Gold: Surface Plasmon Optical Studies of Specific Recognition Reactions. *Langmuir* **1991**, *7*, 1837–1840.
49. Kolomenskii, A. A.; Gershon, P. D.; Schuessler, H. A. Sensitivity and Detection Limit of Concentration and Adsorption Measurements by Laser-Induced Surface-Plasmon Resonance. *Appl. Opt.* **1997**, *36*, 6539–6547.
50. Palik, E. D. In *Handbook of Optical Constants of Solids*; Academic Press: Orlando, FL, 1998.